Suplementary material
Superconductivity-induced change in magnetic anisotropy in epitaxial ferromagnet-superconductor hybrids with spin-orbit interaction

César González-Ruano,[1] Lina G. Johnsen,[2] Diego Caso,[1] Coriolan Tiusan,[3,4] Michel Hehn,[4] Niladri Banerjee,[5] Jacob Linder,[2] and Farkhad G. Aliev[1,*]

[1]*Departamento Física de la Materia Condensada C-III, Instituto Nicolás Cabrera (INC) and Condensed Matter Physics Institute (IFIMAC), Universidad Autónoma de Madrid, Madrid 28049, Spain*

[2]*Center for Quantum Spintronics, Department of Physics, Norwegian University of Science and Technology, NO-7491 Trondheim, Norway*

[3]*Department of Physics and Chemistry, Center of Superconductivity Spintronics and Surface Science C4S, Technical University of Cluj-Napoca, Cluj-Napoca, 400114, Romania*

[4]*Institut Jean Lamour, Nancy Universitè, 54506 Vandoeuvre-les-Nancy Cedex, France*

[5]*Department of Physics, Loughborough University, Epinal Way, Loughborough, LE11 3TU, United Kingdom*

Abstract

In the supplementary material, the section S1 presents a magnetic characterization of the hard Fe/Co layer of the junctions under study. Section S2 presents a magnetic characterization of the soft Fe(001) layer and studies the possible influence of the Meissner screening on the coercive fields of the soft and hard layers. Section S3 estimates the strength of the weak antiferromagnetic coupling between magnetically soft and hard electrodes. Section S4 provides details about the calibration of the angle between the soft and hard layers using the Slonczewski formula, as well as discussing the possible sources of error for this calibration and their magnitude. Section S5 provides an estimation for the magneto-anisotropic energy barrier between the [110] and [100] magnetization directions, normalized per volume or per atom. Section S6 numerically evaluates the possible domain walls pinning by superconducting vortices. Section S7 discusses the contribution of the shape to the magnetic anisotropy. Finally, section S8 provides details on the theoretical modelling of the observed effects.

S1. Magnetic characterizarion of the hard Fe/Co layer

Figure S1 shows the magnetic characterization of the hard Fe/Co bilayer, determined from a typical spin-valve M-H loop on a standard Fe/MgO/Fe/Co single crystal MTJ system (continuous layers, unpatterned). The nominal thickness of the layers on this sample, MgO(100)/Fe(30 nm)/MgO(2 nm)/Fe(10 nm)/Co(20 nm), has been chosen to optimize the magnetic properties of the MTJ stack [1]. The TMR measurements of the coercive fields of the hard ($H_{C,Hard}$) and soft ($H_{C,Soft}$) layers in MTJs under study show that they are well separated from the external field values used to rotate the soft layer. Figure S2 shows that the hard layer switching fields obtained from TMRs along [100], [010] and [110] measured in our junctions remain far above the typical range of 70-120 Oe which is used to rotate the soft layer. Moreover, Figure S3 also shows the typical temperature dependence of $H_{C,Hard}$, demonstrating its independence with temperature from well above to well below T_C.

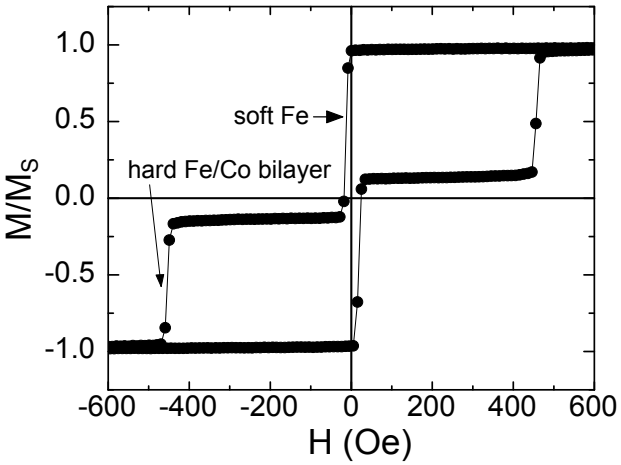

Fig. S 1: Magnetic characterization of a Fe(30 nm)/MgO/Fe(10 nm)Co(20 nm) structure, at room temperature, along the [100] direction.

S2. Magnetic characterizarion of the soft Fe(001) layer and estimation of the Meissner screening

The magnetostatic Meissner screening has been discussed mainly in studies with perpendicular magnetiza-

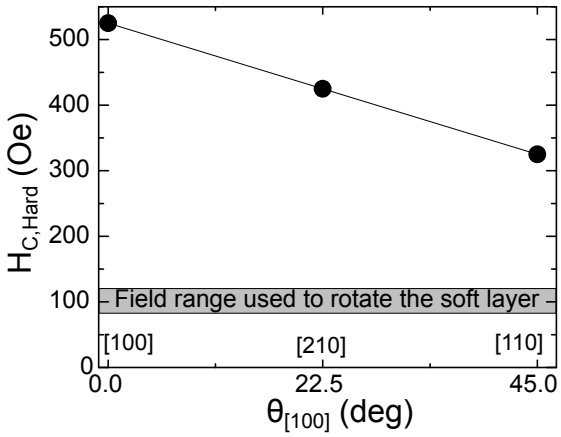

Fig. S2: Coercive field of the hard Fe/Co layer for magnetic field oriented along different crystallographic directions [100], [110] and [210], above the superconducting critical temperature ($T = 5$ K). The grey band shows the typical field range used to manipulate the magnetization of the soft Fe(100) layer in the rotation experiments.

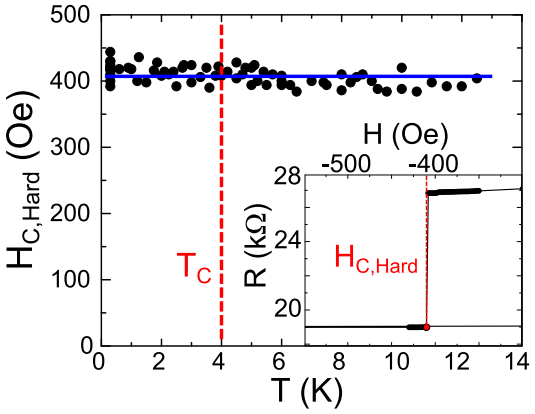

Fig. S3: Typical temperature dependence of the coercitive field of the hard Fe/Co ferromagnetic layer along the [100] direction. The critical temperature is marked with a dashed red line. We relate the excess scatter observed in the hard layer with the extra structural disorder at the Fe/Co interface, providing an enhanced coercive field for the Fe/Co layer. The blue line is a guide for the eye. The inset shows the method for determining the coercive field: it's the field of the first point after the hard layer transition from in each TMR experiment.

tion [2]. In the case of the experiments with in-plane field rotation which we carry out, such field expulsion could induce some screening of the external magnetic field applied to invert or rotate the magnetization of the soft Fe(001) layer (which is the closest to the superconductor), and with less probability affect the switching of the more distant hard Fe/Co layer.

Figure S4 shows the typical variation of the coercive field of the soft Fe(001) ferromagnetic layer with temperature from above to below the critical temperature. We observe some weak increase of the coercive field below 10 Oe, which could be due to spontaneous Meissener screening and/or vortex interaction with domain walls. These changes, however, are an order of magnitude below the typical magnetic fields applied to rotate the Fe(001) layer (70-120 Oe). As we also show in Figure S3, the coercive field of the hard FeCo layer (typically above 400-500 Oe) shows practically no variation (within the error bars) within a wide temperature range, from $3T_C$ to $0.1T_C$, discarding the influence of the Meissner screening on the hard layer.

As the superconducting layer is much larger in area than the ferromagnetic one, these experiments point out that the possible existing Meissner screening would introduce about a 10% correction to the actual external field acting on the soft ferromagnet, regardless of the external field direction.

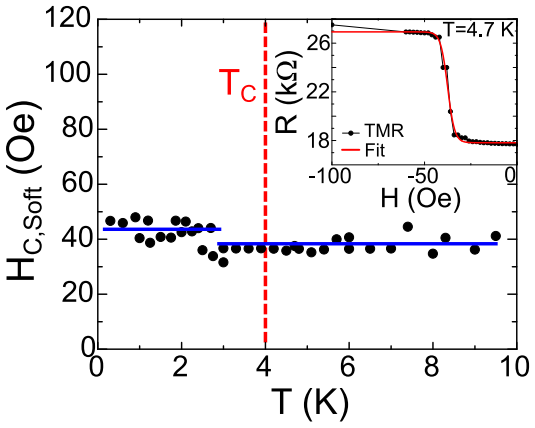

Fig. S4: Typical temperature dependence of the coercitive field of the soft Fe(001) ferromagnetic layer measured along [100] direction. The critical temperature is marked with a dashed red line. Blue lines are guides for the eye. The inset shows the method for determining the coercive field: a logistic fit was performed for the transition, and the coercive field was defined as the mid-height value of the fit.

S3. Estimation of the weak antiferromagnetic coupling of the two ferromagnetic layers.

In order to quantify the unavoidable weak antiferromagnetic magnetostatic coupling between the rotated soft Fe(001) and the practically fixed hard FeCo layer, we show low field TMR measurements where the AP state is achieved and then maintained at zero field (Figure S5a). One clearly observes that the AP and P states can be

obtained as two different non-volatile states, and therefore the antiferromagnetic coupling is not sufficient to antiferromagnetically couple the two layers at zero field. The stability of the P state against the antiferromagnetic coupling is confirmed by the temperature dependence of the resistance in the P and AP states. The P state shows stable resistance values at least below 15 K (Figure S5b). This means that the antiferromagnetic coupling energy is well below 2 mV.

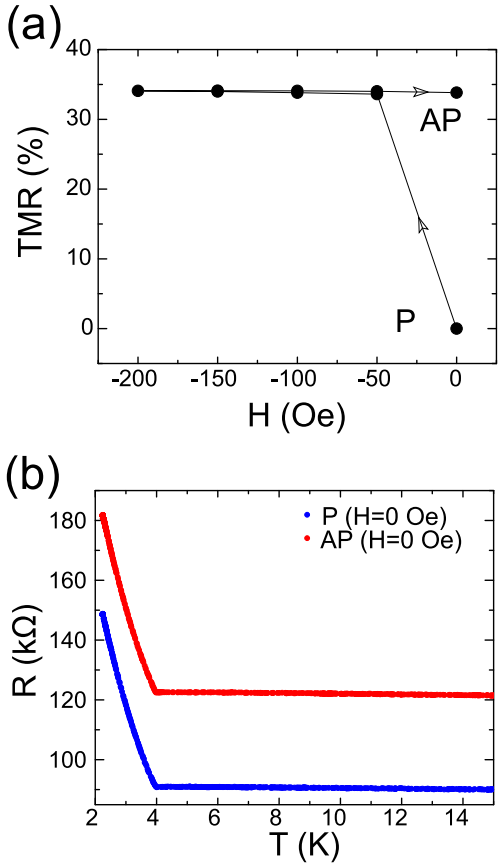

Fig. S5: Two experiments demonstrating the stability of the P and AP states at zero field. (a) TMR to AP state before a critical temperature measurement: the sample was first saturated in the P state with $H = 1000$ Oe in the [100] direction, and then a negative field sweeping was performed to -200 Oe and back to 0 Oe in the same direction in order to switch the soft layer into the AP state, where it remained at zero field. (b) Two critical temperature measurements: the sample was saturated in the P state, and then switched to AP state as described in (a) for the AP measurement. After this, the temperature was risen to 15 K and let to slowly cool down to $T \sim 2$ K. The increase in resistance below 4 K corresponds to the opening and deepening of the superconducting gap, since the voltage used was only a few microvolts in order to distinguish the superconducting transition from its appearance. Both experiments show no sudden changes in resistance, as would happen if any magnetic transition took place.

S4. Calibration of the angle between the two ferromagnetic layers

In order to estimate the angle between the two ferromagnets for the TMR measurements and rotations, we used the Slonczewski model [3]. By using values of the resistance in the AP, P and PIP states established above T_C, we can calculate the desired angle θ with the following expression:

$$G^{-1} = {G_1}^{-1} + \left[G_2\left(1 + p^2\cos\theta\right)\right]^{-1}. \qquad (1)$$

Here, G is the total conductance of the sample, G_1 and G_2 are the conductances of each of the two tunnel barriers, and p is the spin polarization in the ferromagnets, for which we obtain values between 0.7 and 0.8 depending on the sample (the value being robust for each individual one).

In order to ascertain the precission of this calibration method, an analysis of the different errors has been performed. First, an standard error propagation calculation was done to estimate the uncertainty in the resistance values, taking typical values for the current and voltage of 100 nA and 5 mV, respectively, which gives us a typical resistance value of 50 kΩ. The current is applied using a Keithley 220 Current Source, which has an error of 0.3% in the operating range according to the user manual. The voltage is measured using a DMM-522 PCI multimeter card. In the specifications, the voltage precision is said to be 5 1/2 digits. With all this, the resistance error obtained is ΔR=75.08 Ω or a 0.15% of relative error. Using this value, the error bars in the measurements shown in the main text would be well within the experimental points.

For the calculated angle, the error propagation method is not adequate. It gives errors bigger than 360 degrees for some angles, and in general over 30 degrees. This is clearly not what it is observed in reality: the performed fits are quite robust, showing little variance in the estimated angle when changing the input parameters all that is reasonable. Instead, we have used a typical rotation performed on a 30×30 μm^2 sample. The fitting to the Slonczewski formula needs three input values: the resistance in the P state (R_P), the resistance in the AP state (R_{AP}) and the resistance in the PIP state (R_{PIP}). Using these, a numerical algorithm calculates the spin polarization (p), the resistance of the F/F barrier (R_{FIF}), and the resistance of the F/S (F/N) barrier (R_{NIF}). These give us the total resistance of the sample as a function of the angle Φ_{FM} between the two ferromagnets or, reciprocally, the angle as a function of resistance. For our estimation, we have varied the value of the R_{PIP} input parameter from the lowest to the highest possible in the PIP state of the rotation, as well as taking an intermediate value which would be used in a normal analysis

(the P and AP resistance values are always taken as the minimum and maximum resistance values in the rotation respectively). The calculated parameters for the resistance of each barrier and the polarization may slightly vary from one fitting to another, but the overall fitting remains remarkably stable, as shown in Figure 6.

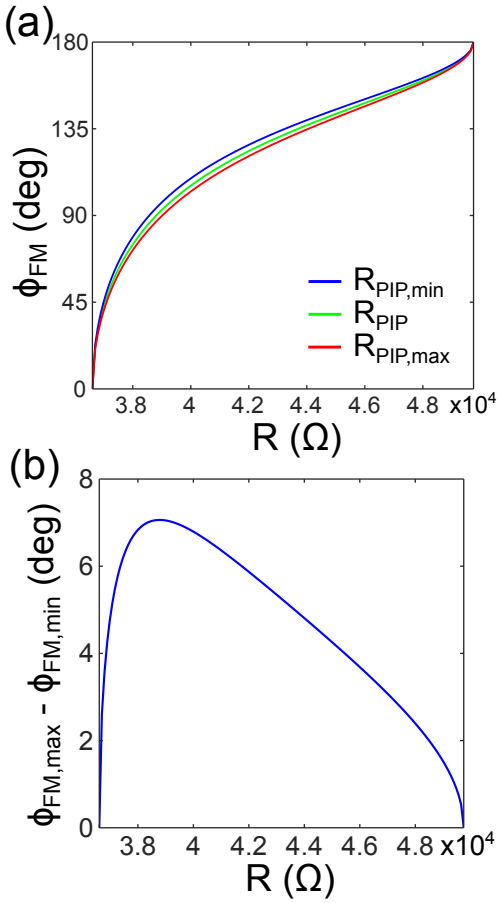

Fig. S6: (a) Φ_{FM} as a function of resistance for the fittings with maximum, usual, and minimum R_{PIP} used, in the P-AP resistance range. (b) difference of calculated angle vs resistance (in the P-AP resistance range) for the fittings with maximum and minimum R_{PIP} used.

As expected, the difference is higher for the PIP state, and minimum in the P and AP state that are "fixed". The difference doesn't exceed 7 degrees, and it keeps below 2 degrees near the P and AP states.

S5. Saturation magnetization for thin Fe(001) films in [100] and [110] directions

Different M vs H measurements were performed at room temperature on a 10 nm thick Fe films, both for the easy [100] and hard [110] crystallographic axes, in order to estimate the magnetocrystalline anisotropy (MCA) energy. The results are depicted in Fig. S7. Using the saturation field for the two directions, the anisotropy energy can be estimated as $K_{Fe} = M_{Fe}H_{Sat}/2 = 5.1 \times 10^5$ erg $\cdot$ cm^{-3}, where $M_{Fe} = 1714$ emu/cm^3 is used. The anisotropy energy per unit cell is therefore MAE= 6.674 μeV, or 3.337 μeV per atom. The obtained energy barrier is similar to the one measured using ferromagnetic resonance [4].

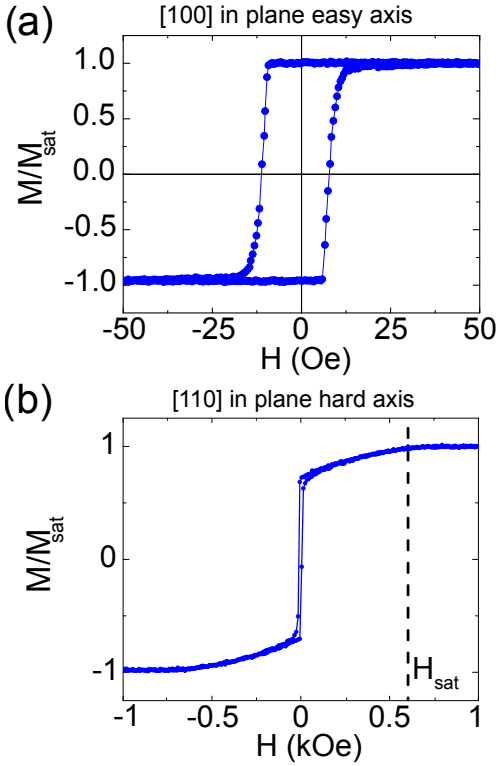

Fig. S7: M vs H measurements on a 10 nm thick Fe film for the easy [100] (a) and hard [110] (b) crystallographic axis. The saturation field (H_{sat}) for the easy axis is around 10 Oe, while for the hard direction it reaches up to 600 Oe.

As shown in Fig.S8, the experimental MCA energy values have been theoretically confronted with theoretical/numerical calculations of the angular in-plane variation of magnetic anisotropy, using the ab-initio Wien2k FP-LAPW code [5]. The calculations were based on a supercell model for a V/MgO/Fe/MgO slab similar to the experimental samples. To insure the requested extreme accuracy in MCA energy values (μeV energy range), a thoroughly well-converged k grid with significantly large number of k-points has been involved. Within these circumstances, our theoretical results for the Fe(001) thin films show standard fourfold anisotropy features and reasonable agreement with the experimentally estimated figures with a maximum theoretical MAE of 4.9 μeV per atom (expected theoretical under-estimation of the magnetocristalline energy within the GGA approach). Note that the superonducting-V induced MCA modulation features cannot be described within the ab-initio

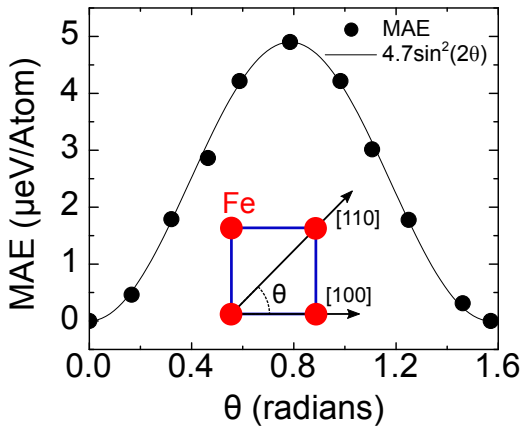

Fig. S 8: Ab-initio calculation of magnetocryscalline anisotropy energy (MAE) as a function of the in-plane orientation angle θ, defined in the inset. Solid line is a phenomenological fit to a $\sin^2(2\theta)$ function.

FP-LAPW approach, describing the V in its normal metallic state. Therefore, the below T_C experimentally observed MCA energy modulations have to be clearly related to the proximity effect in the superconducting V/MgO/Fe(001) system and not to any specific MCA feature of Fe(001) in the V/MgO/Fe(001)/MgO complex stacking sequence.

S6. Evaluation of the vortex induced pinning of domain walls

Using MuMax3 [6], we have compared numerically the DWs formation along the [100] and [110] magnetization directions. The simulations took place in samples with 3×3 μm^2 lateral dimensions (100 nm rounded corners were used as the devices have been fabricated by optical lithography), with $512 \times 512 \times 16$ cells, at $T = 0$. The rest of the parameters used were $A_{ex} = 2.1 \times 10^{-11}$ J/m for the exchange energy, $M_{\rm sat} = 1.7 \times 10^6$ A/m for the saturation magnetization, a damping parameter $\alpha = 0.02$, and crystalline anisotropy parameters $K_{C1} = 4.8 \times 10^4$ J/m^3 and $K_{C3} = -4.32 \times 10^5$ J/m^3. The goal of the simulations was to evaluate the DW formation and their interaction with the superconducting vortices induced by the vertical component of the stray fields at a 2-3 nm from the Fe(001) surface. We observed that, depending on the external field, in the range of 70-1000 Oe both edge-type and inner-type DWs are formed when the field is directed along [100], and mainly edge type DWs are formed with field along [110] (Figure S9a).

We have also calculated the interaction $\mathcal{I}$ between the DW related excess exchange energy $E_{\rm ex}$ and the vertical component of the stray fields, $B_{\rm eff}$ (Figure S9b):

$$\mathcal{I} = \int_0^{N_x} \int_0^{N_y} |B_{\rm eff}|\, E_{\rm ex} \mathcal{F} dx dy \qquad (2)$$

Where N_x and N_y are the total number of cells in each dimension of the simulation, and $\mathcal{F}$ is a filter "Vortex generation function" that takes into account the simulated dependence of the number of vortices on the vertically applied field (Figure S9c). The vortices were simulated using the Time Dependent Ginzburg Landau code developed in Madrid described in [7]. The TDGL simulations took place in 5×5 μm^2 Vanadium samples with 200×200 cells, at $T = 2$ K, with a coherence length $\xi_0 = 2.6 \times 10^{-8}$ based on our experimental estimations for the studied devices, $\kappa = 3$ and $T_C = 4$ K. A uniform field was applied in the perpendicular direction, its magnitude varying from $0.1H_{C2}$ to $0.6H_{C2}$, and the number of vortices generated in the relaxed state were counted.

The second critical field in the vertical direction ($H_{c2} =$ 3 kOe) was determined experimentally. The estimated interaction shows that in the weakly saturated regime, when the inner DWs could emerge and the DW-vortex interaction increases, such interaction should pin the magnetization along the [100] direction, corresponding to the MCA already present in the normal state, therefore blocking any magnetization rotation towards the [110] direction, contrary to our experimental observations. The possible reason for the irrelevance of the DW-vortex interaction in our system is that inner DWs are expected to be of Neel-type for the thickness considered [8].

Finally we mention that our numerical evaluations show that, if present, the vortex-DW interaction should remain dominant for the magnetization directed along [100] respect [110] and for the magnetic field range 70-1000 Oe also without K_{C3} parameter providing the MCA energy minima along [110]. In these simulations the Fe(001) layer has been considered to be smooth. In order to further approach simulations to the experiment, we have also verified that the conclusions above are not affected by the introduction of interfacial magnetic disorder due to mismatch defects (every 30 lattice periods) with 25% excess of Fe moment at the Fe/MgO interface [9]. More detailed simulations involving also interface roughness could be needed to further approach the real experimental situation.

S7. Magnetization alignment along [110] and irrelevance of the junction area for the superconductivity induced MCA modification

As we mentioned in the main text, our experiments point that Fe(001) layers are close to a highly saturated state when the magnetization is directed along [100] or equivalent axes. On the other hand, micromagnetic simulations (Figure S9a) show that the magnetization align-

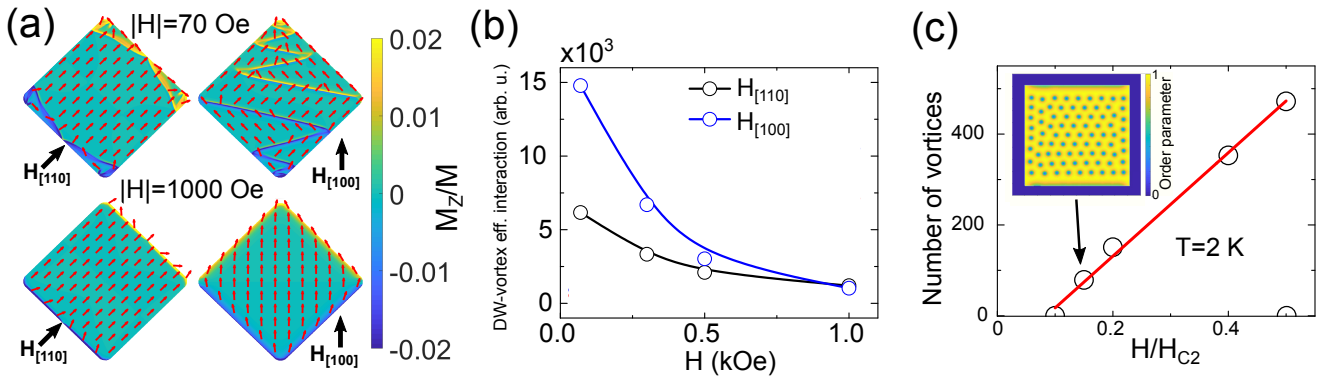

Fig. S9: (a) Typical DW formation mapped by MuMax3 simulations for the [110] and [100] applied field directions in the non-saturated (70 Oe) and saturated (1000 Oe) field regimes. The color map represents the out of plane component of the magnetization, while the red arrows indicate the in plane direction. (b) Values of the 2D integral $\mathcal{I}$ between the local exchange energy (DWs) and the perpendicular component of the stray fields at a distance of 2-3 nm from the ferromagnet, taking into acount the vortex generation function $\mathcal{F}$. (c) Vortex generation function $\mathcal{F}$, represented as number of vortices formed in a 5×5 μm^2 square 40 nm thick superconducting Vanadium film as a function of the applied perpendicular field (normalized by the second critical field H_{c2}), simulated at $T = 2$ K by using the TDGL code described in [7]. The insert shows a typical image of the vortices at H=0.15H_{c2}

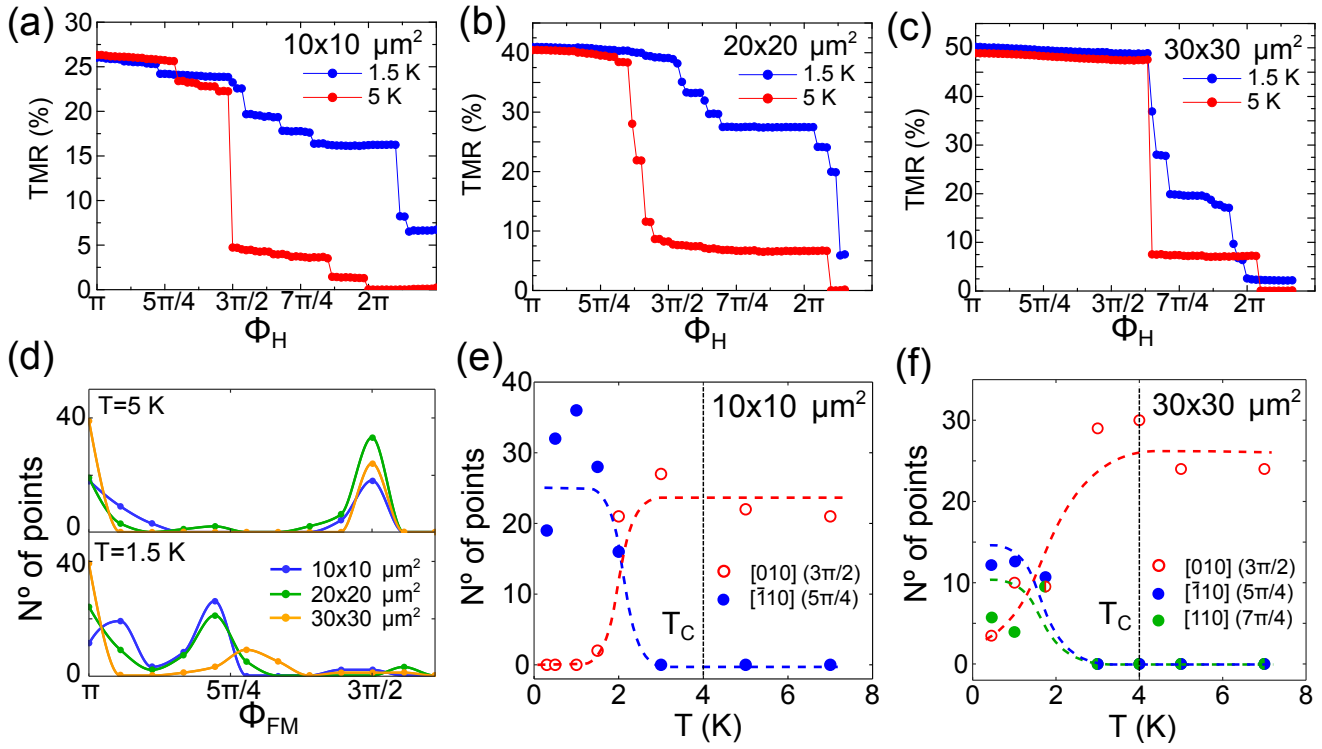

Fig. S10: In-plane field rotation experiments with $H = 70$ Oe below (blue) and above (red) T_C for 10×10 (a), 20×20 (b) and 30×30 (c) μm^2 junctions. (d) Histograms of the calculated angle between the two FM layers ϕ_{FM} for these same rotations, above and below T_C, showing the $[\bar{1}10]$ states for low temperatures. (e) and (f) show the evolution of the [110], $[\bar{1}10]$ and [010] (PIP) states with temperature for the same 10×10 and 30×30 μm^2 junctions (qualitatively simular evolution is shown in Figure 2f in the main text for the 20×20 μm^2 junction).

ment is more robust in the [110] direction (or equivalent) rather than in the [100] direction (or equivalent). So, if we indeed reach a highly saturated state in the [100] direction, this should also be the case for the [110] direction. Therefore, the emergent stable tunneling magnetoresistance states we observe experimentally below T_c, cannot be explained in terms of the intermediate multidomain states but rather correspond to the dominant [110] magnetization alignment of the Fe(001) layer.

As shown in Figure S10, our experiments shows that the observed effects remain qualitatively unchanged when the junction area is varied about an order of magnitude.

S8. Modelling

We describe the V/MgO/Fe structure by the Hamiltonian [10]

$$\begin{aligned} H = &- t \sum_{\langle \boldsymbol{i},\boldsymbol{j}\rangle,\sigma} c^\dagger_{\boldsymbol{i},\sigma} c_{\boldsymbol{j},\sigma} - \sum_{\boldsymbol{i},\sigma} (\mu_{\boldsymbol{i}} - V_{\boldsymbol{i}}) c^\dagger_{\boldsymbol{i},\sigma} c_{\boldsymbol{i},\sigma} \\ &- \sum_{\boldsymbol{i}} U_{\boldsymbol{i}} n_{\boldsymbol{i},\uparrow} n_{\boldsymbol{i},\downarrow} + \sum_{\boldsymbol{i},\alpha,\beta} c^\dagger_{\boldsymbol{i},\alpha} (\boldsymbol{h_i}\cdot\boldsymbol{\sigma})_{\alpha,\beta} c_{\boldsymbol{i},\beta} \\ &- \frac{i}{2} \sum_{\langle \boldsymbol{i},\boldsymbol{j}\rangle,\alpha,\beta} \lambda_{\boldsymbol{i}} c^\dagger_{\boldsymbol{i},\alpha} \hat{n}\cdot(\boldsymbol{\sigma}\times\boldsymbol{d_{i,j}})_{\alpha,\beta} c_{\boldsymbol{j},\beta} \end{aligned} \tag{3}$$

defined on a cubic lattice. The first term describes nearest-neighbor hopping. The second term includes the the chemical potential and the potential barrier at the insulating MgO layers. The remaining terms describes superconducting attractive on-site interaction, ferromagnetic exchange interaction, and Rashba spin-orbit interaction, respectively. These are only nonzero in their respective regions. In the above, t is the hopping integral, $\mu_{\boldsymbol{i}}$ is the chemical potential, $V_{\boldsymbol{i}}$ is the potential barrier that is nonzero only for the MgO layer, $U > 0$ is the attractive on-site interaction giving rise to superconductivity, $\lambda_{\boldsymbol{i}}$ is the local spin-orbit coupling magnitude, $\hat{n}$ is a unit vector normal to the interface, $\boldsymbol{\sigma}$ is the vector of Pauli matrices, $\boldsymbol{d_{i,j}}$ is a vector from site $\boldsymbol{i}$ to site $\boldsymbol{j}$, and $\boldsymbol{h_i}$ is the local magnetic exchange field. The number operator used above is defined as $n_{\boldsymbol{i},\sigma} \equiv c^\dagger_{\boldsymbol{i},\sigma} c_{\boldsymbol{i},\sigma}$, and $c^\dagger_{\boldsymbol{i},\sigma}$ and $c_{\boldsymbol{i},\sigma}$ are the second-quantization electron creation and annihilation operators at site $\boldsymbol{i}$ with spin σ. The superconducting term in the Hamiltonian is treated by a mean-field approach, where we assume $c_{\boldsymbol{i},\uparrow} c_{\boldsymbol{i},\downarrow} = \langle c_{\boldsymbol{i},\uparrow} c_{\boldsymbol{i},\downarrow}\rangle + \delta$ and neglect terms of second order in the fluctuations δ.

We consider a system of size $N_x \times N_y \times N_z$ setting the interface normals parallel to the x axis and assuming periodic boundary conditions in the y and z directions. To simplify notation in the following, we define $i \equiv i_x$, $j \equiv j_x$, $\boldsymbol{i}_{||} = (i_x, i_y)$ and $\boldsymbol{k} \equiv (k_y, k_z)$. We apply the Fourier transform

$$c_{\boldsymbol{i},\sigma} = \frac{1}{\sqrt{N_y N_z}} \sum_{\boldsymbol{k}} c_{i,\boldsymbol{k},\sigma} e^{\mathrm{i}(\boldsymbol{k}\cdot\boldsymbol{i}_{||})} \tag{4}$$

to the above Hamiltonian and use that

$$\frac{1}{N_y N_z} \sum_{\boldsymbol{i}_{||}} e^{\mathrm{i}(\boldsymbol{k}-\boldsymbol{k}')\cdot\boldsymbol{i}_{||}} = \delta_{\boldsymbol{k},\boldsymbol{k}'}. \tag{5}$$

We choose a new basis

$$B^\dagger_{i,\boldsymbol{k}} = [c^\dagger_{i,\boldsymbol{k},\uparrow} \;\; c^\dagger_{i,\boldsymbol{k},\downarrow} \;\; c_{i,-\boldsymbol{k},\uparrow} \;\; c_{i,-\boldsymbol{k},\downarrow}] \tag{6}$$

spanning Nambu×spin space, and rewrite the Hamiltonian as

$$H = H_0 + \frac{1}{2} \sum_{i,j,\boldsymbol{k}} B^\dagger_{i,\boldsymbol{k}} H_{i,j,\boldsymbol{k}} B_{i,\boldsymbol{k}}. \tag{7}$$

Above, the Hamiltonian matrix is given by

$$\begin{aligned} H_{i,j,\boldsymbol{k}} = \epsilon_{i,j,\boldsymbol{k}} \hat{\tau}_3 \hat{\sigma}_0 + \delta_{i,j} \Big[&\mathrm{i}\Delta_i \hat{\tau}^+ \hat{\sigma}_y - \mathrm{i}\Delta_i^* \hat{\tau}^- \hat{\sigma}_y \\ &+ h_i^x \hat{\tau}_3 \hat{\sigma}_x + h_i^y \hat{\tau}_0 \hat{\sigma}_y + h_i^z \hat{\tau}_3 \hat{\sigma}_z \\ &- \lambda_i \sin(k_y) \hat{\tau}_0 \hat{\sigma}_z + \lambda_i \sin(k_z) \hat{\tau}_3 \hat{\sigma}_y \Big], \end{aligned} \tag{8}$$

where Δ_i is the superconducting gap which we solve for self-consistently, $\hat{\tau}_i \hat{\sigma}_j \equiv \hat{\tau}_i \otimes \hat{\sigma}_j$ is the Kronecker product of the Pauli matrices spanning Nambu and spin space, $\hat{\tau}^\pm \equiv (\hat{\tau}_1 \pm i\hat{\tau}_2)/2$, and

$$\begin{aligned} \epsilon_{i,j,\boldsymbol{k}} \equiv &- 2t \left[\cos(k_y) + \cos(k_z)\right] \delta_{i,j} \\ &- t(\delta_{i,j+1} + \delta_{i,j-1}) \\ &- (\mu_i - V_i)\delta_{i,j}. \end{aligned} \tag{9}$$

The constant term in Eq. (7) is given by

$$\begin{aligned} H_0 = &- \sum_{i,\boldsymbol{k}} \left\{ 2t \left[\cos(k_y) + \cos(k_z)\right] + \mu_i - V_i \right\} \\ &+ N_y N_z \sum_i \frac{|\Delta_i|^2}{U_i}. \end{aligned} \tag{10}$$

We absorb the sum over lattice sites in Eq. (7) into the matrix product by defining a new basis

$$W^\dagger_{\boldsymbol{k}} = [B^\dagger_{1,\boldsymbol{k}}, ..., B^\dagger_{i,\boldsymbol{k}}, ..., B^\dagger_{N_x,\boldsymbol{k}}]. \tag{11}$$

Eq. (7) can then be rewritten as

$$H = H_0 + \frac{1}{2} \sum_{\boldsymbol{k}} W^\dagger_{\boldsymbol{k}} H_{\boldsymbol{k}} W_{\boldsymbol{k}}, \tag{12}$$

where

$$H_{\boldsymbol{k}} = \begin{bmatrix} H_{1,1,\boldsymbol{k}} & \cdots & H_{1,N_x,\boldsymbol{k}} \\ \vdots & \ddots & \vdots \\ H_{N_x,1,\boldsymbol{k}} & \cdots & H_{N_x,N_x,\boldsymbol{k}} \end{bmatrix} \tag{13}$$

is Hermitian and can be diagonalized numerically. We obtain eigenvalues $E_{n,\boldsymbol{k}}$ and eigenvectors $\Phi_{n,\boldsymbol{k}}$ given by

$$\begin{aligned} \Phi^\dagger_{n,\boldsymbol{k}} &= [\phi^\dagger_{1,n,\boldsymbol{k}} \quad \cdots \quad \phi^\dagger_{N_x,n,\boldsymbol{k}}], \\ \phi^\dagger_{i,n,\boldsymbol{k}} &= [u^*_{i,n,\boldsymbol{k}} \; v^*_{i,n,\boldsymbol{k}} \; w^*_{i,n,\boldsymbol{k}} \; x^*_{i,n,\boldsymbol{k}}]. \end{aligned} \tag{14}$$

The diagonalized Hamiltonian can be written on the form

$$H = H_0 + \frac{1}{2}\sum_{n,\boldsymbol{k}} E_{n,\boldsymbol{k}}\gamma^\dagger_{n,\boldsymbol{k}}\gamma_{n,\boldsymbol{k}}, \tag{15}$$

where the new quasi-particle operators are related to the old operators by

$$\begin{aligned} c_{i,\boldsymbol{k},\uparrow} &= \sum_n u_{i,n,\boldsymbol{k}}\gamma_{n,\boldsymbol{k}}, \\ c_{i,\boldsymbol{k},\downarrow} &= \sum_n v_{i,n,\boldsymbol{k}}\gamma_{n,\boldsymbol{k}}, \\ c^\dagger_{i,-\boldsymbol{k},\uparrow} &= \sum_n w_{i,n,\boldsymbol{k}}\gamma_{n,\boldsymbol{k}}, \\ c^\dagger_{i,-\boldsymbol{k},\downarrow} &= \sum_n x_{i,n,\boldsymbol{k}}\gamma_{n,\boldsymbol{k}}. \end{aligned} \tag{16}$$

The superconducting gap is given by $\Delta_{\boldsymbol{i}} \equiv U_{\boldsymbol{i}}\langle c_{\boldsymbol{i},\uparrow}c_{\boldsymbol{i},\downarrow}\rangle$. We apply the Fourier transform in Eq. (4) and use Eq. (16) in order to rewrite the expression in terms of the new quasi-particle operators. Also using that $\langle\gamma^\dagger_{n,\boldsymbol{k}}\gamma_{m,\boldsymbol{k}}\rangle = f\big(E_{n,\boldsymbol{k}}/2\big)\delta_{n,m}$, we obtain the expression

$$\Delta_i = -\frac{U_i}{N_y N_z}\sum_{n,\boldsymbol{k}} v_{i,n,\boldsymbol{k}}w^*_{i,n,\boldsymbol{k}}\left[1 - f\left(E_{n,\boldsymbol{k}}/2\right)\right] \tag{17}$$

for the gap, that we use in computing the eigenenergies iteratively. Above, $f\big(E_{n,\boldsymbol{k}}/2\big)$ is the Fermi-Dirac distribution.

Using the obtained eigenenergies, we compute the free energy,

$$F = H_0 - \frac{1}{\beta}\sum_{n,\boldsymbol{k}}\ln(1 + e^{-\beta E_{n,\boldsymbol{k}}/2}), \tag{18}$$

where $\beta = (k_B T)^{-1}$. The preferred magnetization directions are described by the local minima of the free energy. In the main body of the paper, we use this to explain the possible magnetization directions of the soft ferromagnet when rotating an IP external magnetic field over a 2π angle starting at a parallel alignment with the hard ferromagnet.

Other relevant quantities to consider in modelling the experimental system is the superconducting coherence length and the superconducting critical temperature. In the ballistic limit, the coherence length is given by $\xi = \hbar v_F/\pi\Delta_0$, where $v_F = \frac{1}{\hbar}\frac{dE_{\boldsymbol{k}}}{dk}\big|_{k=k_F}$ is the Fermi velocity related to the normal-state eigenenergy $E_{\boldsymbol{k}} = -2t[\cos(k_x) + \cos(k_y) + \cos(k_z)] - \mu$, and Δ_0 is the zero-temperature superconducting gap [11]. The critical temperature is found by a binomial search, where we decide if a temperature is above or below T_c by determining whether $\Delta_{N_x^{\mathrm{S}}/2}$ increases towards a superconducting solution or decreases towards a normal state solution from the initial guess under iterative recalculations of Δ_i. We choose an initial guess with a magnitude very close to zero and with a lattice site dependence similar to that of the gap just below T_c.

In the main plot showing the free energy under IP rotations of the magnetization, we have chosen parameters $t = 1$, $\mu_{\mathrm{S}} = \mu_{\mathrm{SOC}} = \mu_{\mathrm{F}} = 0.9$, $V = 2.1$, $U = 1.35$, $\lambda = 0.4$, $h = 0.8$, $N_x^{\mathrm{S}} = 30$, $N_x^{\mathrm{SOC}} = 3$, $N_x^{\mathrm{F}} = 8$, and $N_y = N_z = 60$. All length scales are scaled by the lattice constant a, all energy scales are scaled by the hopping parameter t, and the magnitude of the spin-orbit coupling λ is scaled by ta. In order to make the system computationally manageable, the lattice size is scaled down compared to the experimental system, however the results should give qualitatively similar results as long as the ratios between the coherence length and the layer thicknesses are reasonable compared to the experimental system. For this set of parameters, the superconducting coherence length is approximately $0.6N_x^{\mathrm{S}}$. Since the coherence length is inversely proportional to the superconducting gap, U has been chosen to be large in order to allow for a coherence length smaller than the thickness of the superconducting layer. Although this results in a large superconducting gap, the modelling will qualitatively fit the experimental results as long as the other parameters are adjusted accordingly. We therefore choose the local magnetic exchange field so that $h \gg \Delta$, as in the experiment. For this parameter set, $h \approx 20\Delta$. The order of magnitude of λ is 1 eVÅ, given that $t \sim 1$ eV and $a \sim 4$ Å. This is realistic considering Rashba parameters measured in several materials [12]. The Rashba spin-orbit field at the interfaces of V/MgO/Fe is caused by a structural inversion asymmetry across the MgO layer, and breaks the inversion symmetry at the MgO interfaces [13]. This causes generation of triplet-superconductivity even for weakly spin-polarized ferromagnets with a small spin-orbit field [14]. We are therefore not dependent upon a strong magnetic exchange field and a strong spin-orbit field for realizing the observed effects. For the AF coupling contribution to the free energy, we set $f_{\mathrm{AF}} = 0.01$ in order to fit the anisotropy of the experimental system just above T_{C}.

* e-mail: farkhad.aliev@uam.es

[1] C. Tiusan, F. Greullet, M. Hehn, F. Montaigne, S. Andrieu and A. Schuhl, Spin tunnelling phenomena in single-crystal magnetic tunnel junction systems, Journal of Physics: Condensed Matter, **19**, 16 (2007).

[2] L. N. Bulaevskii and E. M. Chudnovsky, Ferromagnetic film on a superconducting substrate, Phys. Rev. B **63**, 012502 (2000).

[3] J. C. Slonczewski, Conductance and exchange coupling of two ferromagnets separated by a tunneling barrier. Phys. Rev. B **39**, 6995 (1989).

[4] A. N. Anisimov, M. Farle, P. Poulopoulos, W. Platow, K. Baberschke, P. Isberg, R. Wäppling, A. M. N. Niklasson and O. Eriksson, Orbital Magnetism and Magnetic

Anisotropy Probed with Ferromagnetic Resonance, Phys. Rev. Lett. **82**, 2390 (1999).
[5] P. Blaha, K.Schwarz, F. Tran, R. Laskowski, G.K.H. Madsen and L.D. Marks, An APW+lo program for calculating the properties of solids, J. Chem. Phys. **152**, 074101 (2020).
[6] A. Vansteenkiste, J. Leliaert, M. Dvornik, M. Helsen, F. Garcia-Sanchez and B. Van Waeyenberge, The design and verification of MuMax3, AIP Advances **4**, 107133 (2014).
[7] A. Lara, C. González-Ruano and F.G.Aliev, Time-dependent Ginzburg-Landau simulations of superconducting vortices in three dimensions, Low Temperature Physics **46**, 316 (2020).
[8] A. Hubert and R. Schäfer, Magnetic domains. The analysis of magnetic microstructures (Springer, Berlin, 1999).
[9] E. Jal et al; Interface Fe magnetic moment enhancement in MgO/Fe/MgO trilayers, Appl. Phys. Lett. **107**, 092404 (2015).
[10] L. G. Johnsen, N. Banerjee, and J. Linder, Magnetization reorientation due to the superconducting transition in heavy-metal heterostructures, Phys. Rev. B **99**, 134516 (2019).
[11] J. Bardeen, L. N. Cooper and J. R. Schrieffer, Theory of Superconductivity, Phys. Rev. **108**, 1175 (1957).
[12] A. Manchon, H. C. Koo, J. Nitta, S. M. Frolov, and R. A. Duine, New perspectives for Rashba spin–orbit coupling, Nat. Mater. **14**, 871 (2015).
[13] I. Martínez, P. Högl, C. González-Ruano, J. P. Cascales, C. Tiusan, Y. Lu, M. Hehn, A. Matos-Abiague, J. Fabian, I. Žutić and F. G. Aliev, Interfacial Spin-Orbit Coupling: A Platform for Superconducting Spintronics, Phys. Rev. Appl. **13**, 014030 (2020).
[14] T. Vezin, C. Shen, J. E. Han, and I. Žutić, Enhanced spin-triplet pairing in magnetic junctions with *s*-wave superconductors, Phys. Rev. B, **101**, 014515 (2020).